Combined interpretation of radar, hydraulic, and tracer data from a fractured-rock aquifer near Mirror Lake, New Hampshire, USA

Frederick D. Day-Lewis · John W. Lane · Steven M. Gorelick

Abstract An integrated interpretation of field experimental cross-hole radar, tracer, and hydraulic data demonstrates the value of combining time-lapse geophysical monitoring with conventional hydrologic measurements for improved characterization of a fractured-rock aquifer. Time-lapse difference-attenuation radar tomography was conducted during saline tracer experiments at the US Geological Survey Fractured Rock Hydrology Research Site near Mirror Lake, Grafton County, New Hampshire, USA. The presence of electrically conductive saline tracer effectively illuminates permeable fractures or pathways for geophysical imaging. The geophysical results guide the construction of three-dimensional numerical models of ground-water flow and solute transport. In an effort to explore alternative explanations for the tracer and tomographic data, a suite of conceptual models involving heterogeneous hydraulic conductivity fields and rate-limited mass transfer are considered. Calibration data include tracer concentrations, the arrival time of peak concentration at the outlet, and steady-state hydraulic head. Results from the coupled inversion procedure suggest that much of the tracer mass migrated outside the three tomographic image planes, and that solute is likely transported by two pathways through the system. This work provides basic and site-specific insights into the control of permeability heterogeneity on ground-water flow and solute transport in fractured rock.

Resumen Una interpretación integrada de radar experimental de campo transversal a pozos, trazadores, y datos hidráulicos demuestra el valor de combinar el monitoreo geofísico realizado en periodos de tiempo con mediciones hidrológicas convencionales en la caracterización mejorada de un acuífero rocoso fracturado. Se llevó a cabo tomografía de radar por periodos de tiempo y diferencia de atenuación durante un experimento con trazadores salinos en el sitio de investigación hidrológica de roca fracturada del Servicio Geológico de Estados Unidos cerca del Lago Espejo, Condado Grafton, New Hampshire, USA. La presencia del trazador salino eléctricamente conductivo refleja efectivamente fracturas permeables o trayectorias para imágenes geofísicas. Los resultados geofísicos orientan la construcción de modelos numéricos tri-dimensionales de flujo de agua subterránea y transporte de solutos. En un esfuerzo por explorar explicaciones alternativas para los datos tomográficos y trazadores se considera un conjunto de modelos conceptuales que involucran campos de conductividad hidráulica heterogéneos y transferencias de masa de ritmo limitado. La calibración de datos incluye concentraciones de trazadores, el tiempo de llegada de la concentración pico en la salida, y presión hidráulica en régimen permanente. Los resultados del procedimiento de acoplamiento invertido sugieren que mucho de la masa del trazador migró fuera de los tres planos de imagen tomográfica, y que el soluto es probablemente transportado por dos trayectorias a través del sistema. Este trabajo aporta ideas básicas y específicas del sitio en relación con el control de la heterogeneidad de permeabilidades en el flujo de agua subterránea y transporte de solutos en rocas fracturadas.

Résumé Une interprétation intégrée d'études de terrain (radar entre puits, traçages, données hydrauliques) démontre la valeur de la combinaison entre la géophysique des temps finis et les mesures hydrologiques conventionnelles pour une interprétation améliorée d'un aquifère

Received: 17 September 2003 / Accepted: 5 July 2004
Published online: 17 September 2004

F. D. Day-Lewis (✉)
Department of Geology,
Bucknell University,
Lewisburg, PA 17837, USA
e-mail: daylewis@usgs.gov
Tel.: +1-860-4877402 ext. 21
Fax: +1-860-487-8802

J. W. Lane Jr
Branch of Geophysics,
US Geological Survey, Office of Groundwater,
Branch of Geophysics,
Storrs, CT 06269, USA

S. M. Gorelick
Department of Geological and Environmental Sciences,
Stanford University,
Stanford, CA 94305, USA

Present address:
F. D. Day-Lewis, US Geological Survey, Office of Ground Water,
Branch of Geophysics,
11 Sherman Place, Unit 5015, Storrs, CT 06269, USA

 DOI 10.1007/s10040-004-0372-y

de roche fracturée. La tomographie au radar a été mise en œuvre durant un traçage artificiel au sel au site de recherche sur l'hydrologie des roches fracturées du Service Géologique des US, à proximité du Lac Mirror, Conté de Grafton, Nouvel Hampshire, USA. La présence du traceur électriquement conducteur met en relief, grâce à la géophysique, la présence de fractures ou d'écoulements préférentiels. Les résultats de la géophysique ont permis la construction de modèle hydrogéologique tri-dimensionnel des écoulements et du transport de soluté. Dans l'optique d'explorer des interprétations alternatives des données de traçage et de tomographie, différents modèles conceptuels sont utilisés concernant l'hétérogénéité des conductivités hydrauliques et des taux limités de transferts de solutés. Les données du calibrage incluent les données de concentration du traceur, le temps d'arrivée du pic de restitution et les données piézométriques en régime permanent. Les résultats de la procédure d'inversion couplée suggèrent qu'une quantité très importante du traceur migre au delà de la fenêtre de visualisation des tomographies, et que le soluté est transporté via deux voies d'écoulement préférentiel. Ce travail apporte des connaissances de base et spécifiques au site concernant la distribution de la perméabilité dans l'aquifère et le transport de soluté dans les roches fracturées.

Keywords Fractured rocks · Geophysical methods · Groundwater flow · Inverse modeling · Tracer tests

Introduction

Accurate and reliable characterization of spatially variable, field-scale hydraulic properties in fractured rock is one of the most difficult problems in hydrogeology. Conventional hydraulic and tracer data are typically insufficient to identify the three-dimensional (3-D) geometry of permeable fractures and fracture zones. The combination of radar tomography and saline tracer tests has been useful for identifying permeable fractures and fracture zones at several research sites (Olsson et al. 1991, 1992; Lane et al. 2000; Day-Lewis et al. 2003). In radar tomography, high-frequency electromagnetic waves propagate from multiple transmitter locations in one borehole and are recorded at multiple receiver locations in a second borehole. From the recorded waveforms, quantities such as first arrival time and amplitude are calculated and used to invert for cross-sectional images of radar slowness (reciprocal velocity) and attenuation, respectively. The presence of electrically conductive saline tracer serves to increase EM-wave attenuation, and thus illuminate permeable pathways for imaging by radar tomography. Plots of radar attenuation versus time can be interpreted as surrogate data for tracer-breakthrough curves (e.g., Binley et al. 1996; Slater et al. 2000; Day-Lewis et al. 2003); thus, in addition to information regarding the spatial configuration of flow paths, time-lapse tomography can provide estimates of tracer arrival times in tomographic image planes.

This paper presents a combined interpretation of tracer and cross-hole radar difference-attenuation data from the US Geological Survey Fractured Rock Hydrology Research Site, near Mirror Lake, New Hampshire. Cross-hole radar data were collected in three adjoining planes during a series of tracer tests in a previously identified fracture zone. The time-lapse series of tomograms provide valuable information about the migration of saline tracer. The geophysical results, reported previously by Day-Lewis et al. (2003), are used in this study to (1) identify promising zonations of the heterogeneous hydraulic-conductivity field, and (2) infer the timing of peak tracer concentration in the image planes.

Although the relation between difference attenuation and concentration may be non-linear (Lane et al. 1998), one would expect the timing of peak concentration to correspond to the timing of peak attenuation at a given location; however, for the field experimental data considered here, the interpretation of the timing of peak difference attenuation was not straightforward. The peak difference attenuation in one of the image planes appeared later than the arrival of peak concentration at the outlet. Three alternative conceptual models to explain the field data are considered, involving combinations of heterogeneity in hydraulic conductivity (K) and rate-limited mass transfer (RLMT). A suite of ground-water flow and solute transport models is constructed and calibrated using non-linear regression with (1) measured concentrations at the extraction well, (2) the timing of peak discharge concentration, and (3) steady-state hydraulic head at the extraction well. Simulated concentrations in the image plane are then compared with nodal difference-attenuation histories from the tomograms to assess consistency with the geophysical data.

Field Experiment

The experimental data used in this study come from the US Geological Survey (USGS) Fractured Rock Hydrology Research Site, near Mirror Lake, New Hampshire, shown in Fig. 1. Fractured-rock research at the site includes studies of field-scale solute transport (Becker and Shapiro 2000; Shapiro 2001; Becker and Shapiro 2003), the relation between seismic tomograms and aquifer properties (Ellefsen et al. 2002), fracture-zone geometry (Day-Lewis et al. 2000), regional ground-water flow (Tiedeman et al. 1998), and interpretation of well-test data (Tiedeman and Hsieh 2001). This paper reports on numerical modeling based on results of concurrent radar and tracer experiments conducted in a four-well cluster at the northeast corner of the Forest Service East (FSE) well field (Lane et al. 1998, 2000; Day-Lewis et al. 2003). About 20 m of glacial deposits overlay the bedrock, which consists of schist intruded by granite, pegmatite, and lamprophyre. Based on analysis of hydraulic data, four major zones of transmissive fractures were identified at the FSE well field (Hsieh and Shapiro 1996). The four zones appear to be tabular, sub-horizontal regions with

 DOI 10.1007/s10040-004-0372-y

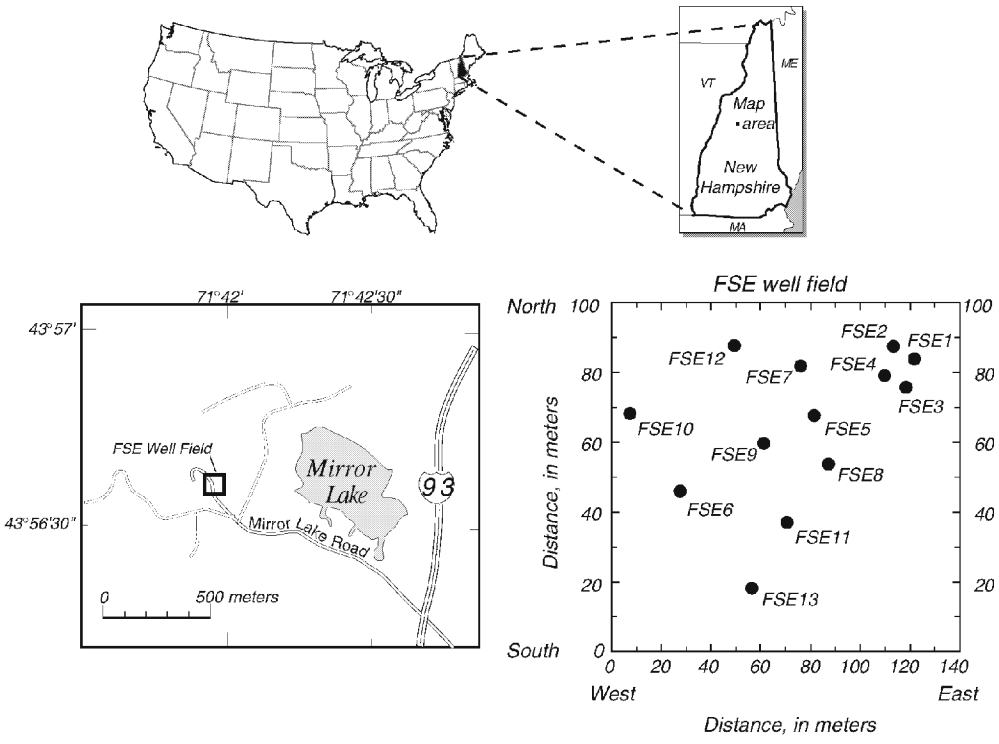

Fig. 1 Map of the US Geological Survey Fractured Rock Hydrology Research Site near Mirror Lake, in Grafton County, New Hampshire, USA

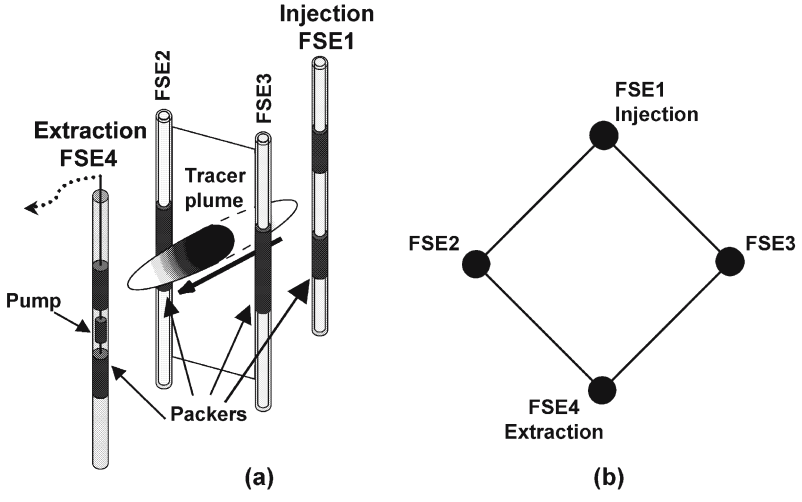

Fig. 2. a Cross section and **b** plan view of the experimental setup for the cross-hole radar and tracer experiments (after Day-Lewis et al. 2003). Tracer injection was in FSE1, extraction was from FSE4, and tomographic imaging was in the FSE1–FSE2, FSE2–FSE3, and FSE3–FSE1 planes

hydraulic conductivity about 3–4 orders of magnitude higher than that of the surrounding bedrock (Hsieh et al. 1999). Day-Lewis et al. (2000) combined geostatistical simulation and non-linear regression with hydraulic-head data to assess the likely extents, shapes, and hydraulic properties of the four zones. One goal of this study is to achieve a more detailed description of the internal architecture and hydraulics of one fracture zone using high-resolution geophysical data than previously possible using hydraulic data alone.

A series of doublet tracer tests was conducted between FSE1 and FSE4 (Fig. 1), with injection of 1.9 L/min in FSE1 and extraction of 3.8 L/min from FSE4. The sodium-chloride tracer was injected at a concentration of 50 g/L NaCl for a period of 10 min, after which injection was switched back to freshwater. Injection and pumping intervals were isolated using inflatable straddle packers, shown in Fig. 2. Cross-hole radar data were collected in the FSE1–FSE2, FSE2–FSE3, and FSE3–FSE1 planes in 10-min intervals. The tracer injection and extraction were within a previously identified fracture zone at a depth of about 45 m (Hsieh and Shapiro 1996). The time-lapse radar data were inverted using a sequential space–time inversion approach (Day-Lewis et al. 2002). This approach capitalizes on temporal correlation to help regularize the inversion and accounts for precise measurement times and changes in attenuation that occur during data collection. Day-Lewis et al. (2003) provide additional details about the experiments, tomographic inversion, and geophysical results. Six time-lapse tomograms are shown

 DOI 10.1007/s10040-004-0372-y

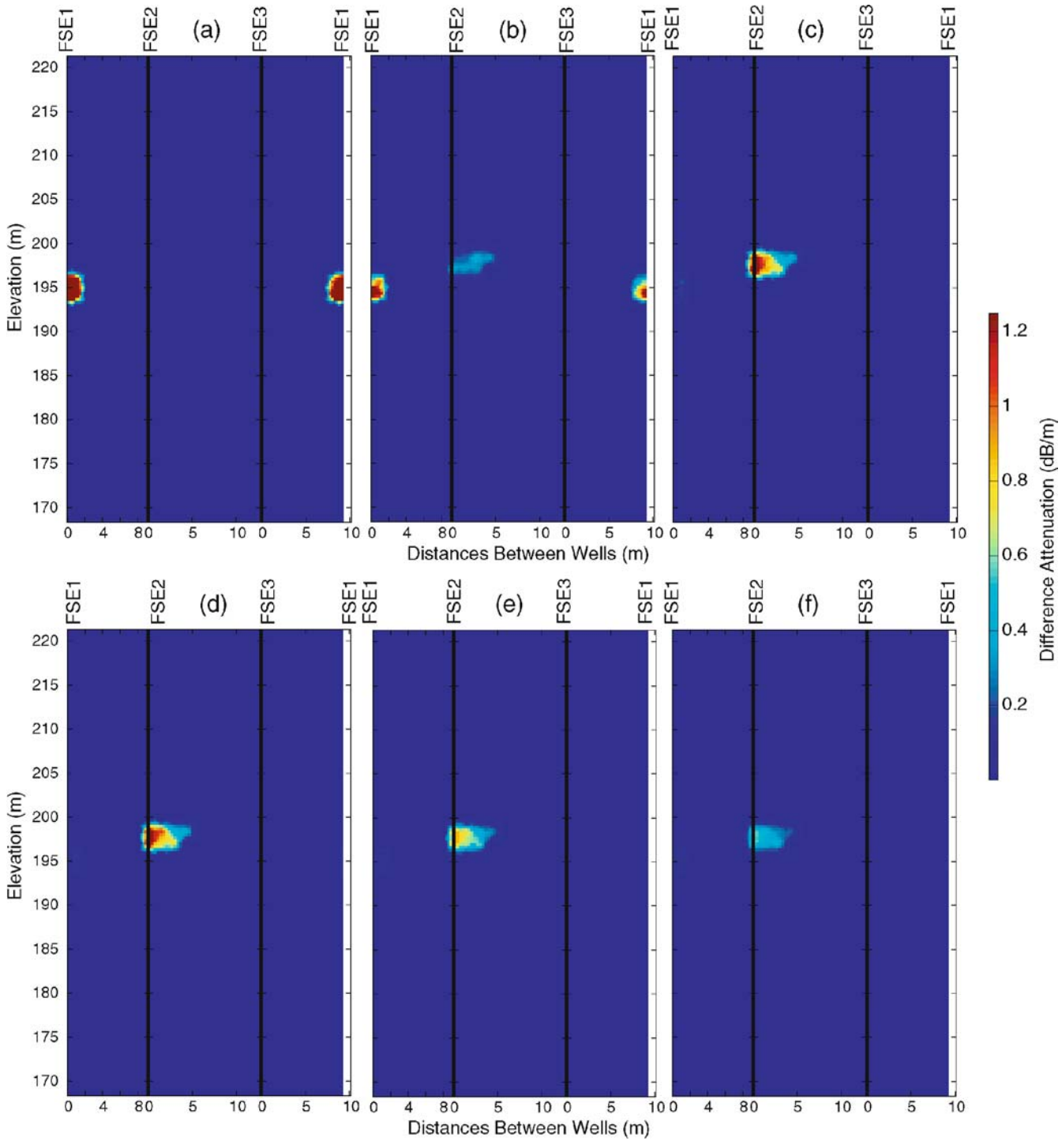

Fig. 3. a 20-min, **b** 50-min, **c** 90-min, **d** 120-min, **e** 150-min, and **e** 200-min difference-attenuation tomograms from constrained inversion (after Day-Lewis et al. 2003)

in Fig. 3. Nodal difference-attenuation histories and the measured tracer concentration at the outlet are compared in Fig. 4. Each black line in Fig. 4 represents a time-series of the increase in attenuation relative to background for a particular pixel in the FSE2–FSE3 image plane; thus, each time-series is a surrogate tracer breakthrough curve.

The first radar detection of tracer in the FSE2–FSE3 plane (30–40 min) is reasonable compared to first detection in outlet discharge at FSE4 (~50 min; Fig. 4), but the timing of the peak difference attenuation is problematic. First, nodal difference-attenuation histories indicate the tracer peak passes through the FSE2–FSE3 plane between 90 and 100 min after the start of injection,

 DOI 10.1007/s10040-004-0372-y

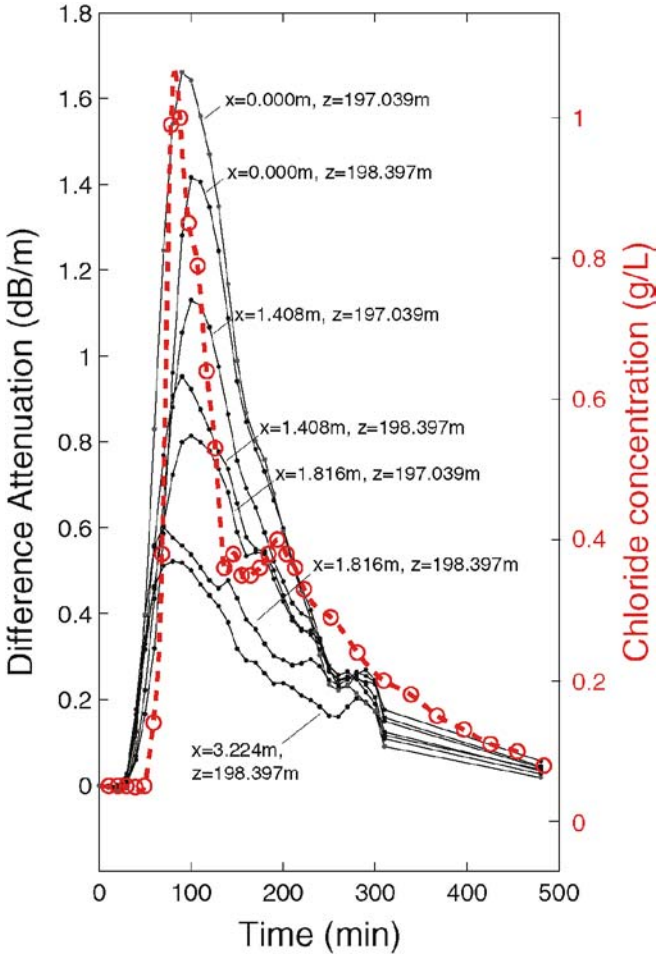

Fig. 4 Nodal difference-attenuation histories in the FSE2–FSE3 plane (*in black*), tracer concentration data (*red circles*) with interpolated concentrations (*dashed red line*)

but the peak tracer concentration at the outlet occurs earlier, at about 77 min. Second, comparison of the breakthrough curve at the outlet to the attenuation breakthrough curves in the image plane indicates that the latter are broader; however, the effect of dispersion ought to be less at intermediate points along a flowpath. A series of numerical modeling experiments were conducted in an effort to explain these apparent discrepancies.

Methods

Radar Tomography

Cross-hole seismic and radar geotomography (Dines and Lytle 1979; Nolet 1987) are similar to the CT-scan technology used in medical imaging. In radar tomography, high-frequency electromagnetic waves are propagated from transmitter locations in one borehole to receiver locations in a second borehole. Waveform traces are recorded at receiver locations, and quantities such as travel time, energy, or amplitude are calculated for each transmitter-receiver raypath. Inversion produces a cross-sectional image of radar slowness in the case of travel-time data, or an image of radar attenuation in the cases of amplitude or energy data. Because radar attenuation is a strong function of electrical conductivity and therefore salinity, difference-attenuation tomography is effective for monitoring saline tracer transport (Olsson et al. 1991; Lane et al. 1998, 2000; Binley et al. 2001; Hubbard et al. 2001; Day-Lewis et al. 2003). In the case where wave propagation dominates over conduction, radar attenuation is given by:

$$\alpha \approx 0.163\sigma/\sqrt{\varepsilon_r} \qquad (1)$$

where α is the attenuation, in dB/m, ϵ_r is the relative dielectric permittivity, and σ is electrical conductivity, in μS/cm. According to Eq. (1), radar attenuation increases with electrical conductivity, which increases with pore-fluid salinity (Archie 1942).

The geophysical data and tomograms considered here were inverted on a 4-D nodal mesh using a sequential least-squares approach to time-lapse tomography (Day-Lewis et al. 2002). The inversion employs space–time parameterization and regularization and accounts for temporal variations in attenuation that occur during data collection. Given the offset and vertical extent of the boreholes bounding a tomogram, the theoretical vertical and horizontal resolution limits for transmission tomography can be estimated using the formulae of Schuster (1996). In the FSE2–FSE3 planes, the horizontal resolution is estimated to be 1.3 m and the vertical resolution to be 2.9 m. It should be noted that other factors including measurement error, regularization and finite ray coverage degrade resolution. In practice, the available data are typically insufficient to estimate all parameters independently, the inverse problem is underdetermined, regularization is required, and tomographic estimates represent local averages rather than point estimates (e.g., Day-Lewis and Lane 2004). Thus, estimates of difference attenuation are spatial (and temporal) averages that may be sensitive to multiple flowpaths with different arrival times and concentration histories. Local averaging over multiple flowpaths may also result in a time lag between peak concentration and peak radar attenuation, which may serve to increase the spread of difference-attenuation breakthrough as illustrated for a hypothetical case in Fig. 5. Consequently, comparison of difference-attenuation breakthrough curves and measured solute concentration histories is not straightforward.

The degree of local averaging due to insufficient data can be evaluated by examination of the model resolution matrix, **R** (Menke 1989). **R** depends on the data configuration, the forward model of physical process underlying the measurements, the model of data errors, and prior information used to regularize the inversion. The resolution matrix can be conceptualized as the lens or filter through which the tomographic survey sees the earth (Vasco et al. 1997). For the case of difference-attenuation tomography, **R** relates the vector of difference-attenuation estimates, $\mathbf{\Delta\alpha}$, to the true difference attenuation, $\mathbf{\Delta\alpha}$:

 DOI 10.1007/s10040-004-0372-y

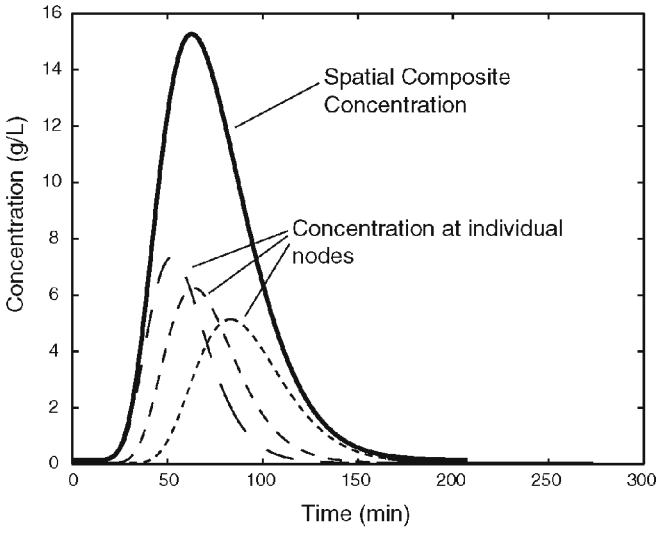

Fig. 5 Schematic diagram showing hypothetical tracer concentration breakthrough curves at points on several flow paths, and the spatial composite (sum) breakthrough curve

$$\Delta\hat{\boldsymbol{\alpha}} = \mathbf{R}\,\Delta\boldsymbol{\alpha} \tag{2}$$

Thus, the i^{th} row of **R** describes the resolution of the i^{th} parameter; i.e., $\Delta\hat{\alpha}_i$ is an average of other parameters in the image plane, with the influence of parameter j given by R_{ij}. In the case of perfect model resolution (an over determined problem), **R** is an identity matrix and all parameters are resolved uniquely. More typically, there are non-zero off-diagonal elements.

The model resolution matrix is a powerful tool for predicting the inversion results for hypothetical scenarios involving different transmitter-receiver geometries, regularization criteria, data quality, synthetic models, etc. In this study, **R** is used to facilitate comparison of tomographic difference-attenuation histories and measured solute concentrations. Whereas the latter are essentially point measurements, the former are local averages (in space and time) with the averaging process controlled by the model resolution matrix; thus, **R** can be used to upscale concentrations to yield quantities appropriate for comparison with tomograms.

For time-lapse inversion, difference-attenuation estimates in the k^{th} tomogram, $\Delta\hat{\boldsymbol{\alpha}}^k$, are based on several sets of data collected over a temporal window; thus, $\Delta\hat{\alpha}_i^k$ depends on parameter difference attenuation at other nodes within a space–time neighborhood. The resolution matrix is calculated according to the approach presented in Day-Lewis et al. (2002). The row of the model resolution matrix corresponding to the highest difference-attenuation node in the FSE2–FSE3 plane is shown in Fig. 6. This plot illustrates that estimation of difference attenuation involves spatial and temporal averaging with nodes in a neighborhood with a radius of several meters and temporal window of 20 min.

To enhance resolution, ray-based constraints were applied in the inversion to limit the difference-attenuation anomalies to regions of the tomograms traversed by a high proportion of ray paths exhibiting large positive changes in attenuation. Nodes outside these regions are constrained to a difference attenuation of zero. The resulting improvement in model resolution comes at the expense of not resolving parameters outside the active region. In the field experiment, time constraints severely limited the number of rays collected in each time-lapse data set. The use of such severe constraints was necessary to suppress streak artifacts unwarranted by the data.

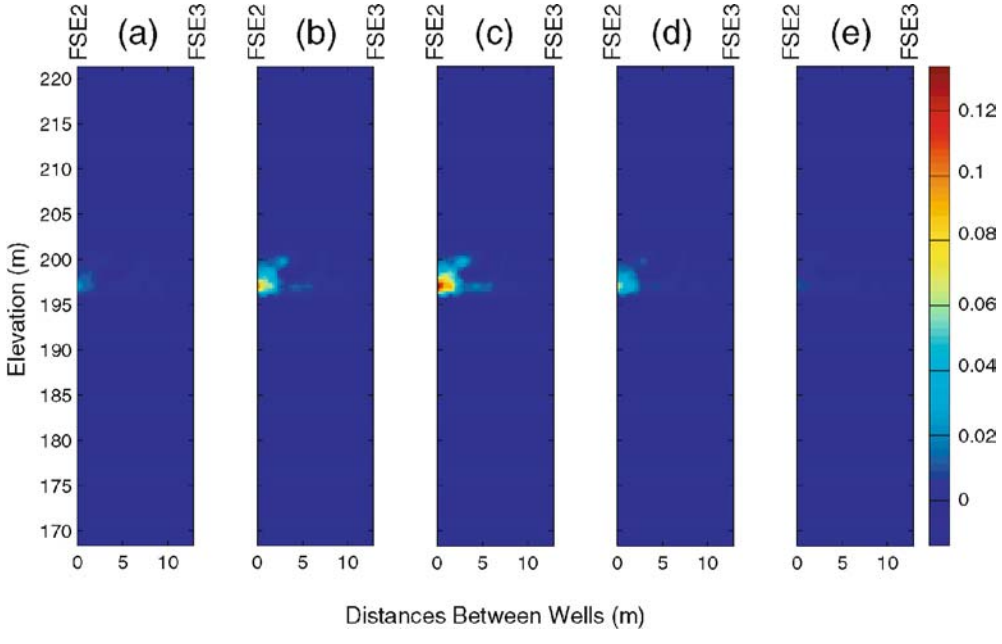

Fig. 6 Resolution of the highest attenuation node (x=0.65 m, y=197 m) in the FSE2–FSE3 image plane in the k-time mesh, with respect to parameters at time *a* k-2, *b* k-1, *c* k, *d* k+1, and *e* k+2. The higher the value at a given location, the greater the estimation is influenced by that location

 DOI 10.1007/s10040-004-0372-y

Numerical Modeling of Ground-water Flow and Solute Transport

Ground-water flow and solute transport were simulated using a finite-element model (Gandhi et al. 2002). The governing equations are those of steady-state three-dimensional ground-water flow [Eq. (3)], Darcy's Law and average linear pore velocity [Eq. (4a, 4b)], and transient advective–dispersive solute transport with, in some scenarios considered, first-order rate-limited mass transfer between mobile and immobile domains [Eq. (5a, 5b)]:

$$\frac{\partial}{\partial x_i}\left(K_{ij}\frac{\partial h}{\partial x_j}\right) + Q_s(x) = 0 \tag{3}$$

$$q_i = -K_{ij}\frac{\partial h}{\partial x_j} \tag{4a}$$

$$v_i = \frac{q_i}{\theta_m} \tag{4b}$$

$$\frac{\partial}{\partial x_i}\left(D_{ij}\frac{\partial C_m}{\partial x_j}\right) - v_i\frac{\partial C}{\partial x_i} + \frac{Q_s(x)}{\theta_{im}}(C_s - C_m) - \frac{\lambda}{\theta_m}(C_m - C_{im})\frac{\partial C_m}{\partial t} = 0 \tag{5a}$$

$$\frac{\lambda}{\theta_{im}}(C_m - C_{im}) - \frac{\partial C_{im}}{\partial t} = 0 \tag{5b}$$

where h is hydraulic head, K_{ij} are elements of the hydraulic conductivity tensor, $Q_s(\mathbf{x})$ is the flow rate per unit volume of sources or sinks at spatial location $\boldsymbol{x}$, x_i is the spatial Cartesian coordinate direction i, q_i is the specific discharge in direction i, C is concentration, D_{ij} are elements of the dispersion tensor, v_i is the average linear pore velocity in direction i, t is time, C_s is the concentration of the source or sink, λ is the rate constant for mass transfer between the mobile and immobile domains, θ_m is the mobile-domain porosity, and θ_{im} is the immobile-domain porosity.

The boundary conditions for flow are zero drawdown (constant head) at the top of the mesh, corresponding to an interface with high-K overburden material, and zero-gradient (no-flow) boundaries on all other sides. These boundary conditions correspond to a situation where primarily vertical flow occurs in the low-K bedrock, and horizontal flow occurs in the high-K fracture zone. The mesh extends 40 m in the horizontal directions and 23.5 m vertically. Different finite-element meshes were used for ground-water simulation in each scenario, with each consisting of about 20,000 nodes and 35,000 to 40,000 elements. The lateral dimensions of the fracture zone are consistent with geostatistical simulations of its likely extent (Day-Lewis et al. 2000). Following Hsieh et al. (1999), the zone is assumed to be 1.5 m thick. The various high- and low-K features considered in this paper are assumed to be embedded within this 1.5-m thick high-K layer. Boundary conditions for transport are zero gradient on all sides, and the initial condition is 0.05 g/L everywhere based on the concentration measurements preceding each tracer experiment. Salinity in the four-well cluster was elevated due to previous saline tracer experiments.

Shapiro (1996) estimated effective porosity to be 0.001 for the site. Based on multiple-well pumping tests, Hsieh et al. (1999) estimated the vertical and horizontal hydraulic conductivities of the low-K bedrock to be about $4.0\text{x}10^{-7}$ m/s and $1.8\text{x}10^{-8}$ m/s, respectively. In this paper, the horizontal K of the bedrock is assumed to be $1.8\text{x}10^{-8}$ m/s. Hsieh et al. (1999) estimated the hydraulic conductivity of fracture zones to be $2.0\text{x}10^{-4}$ m/s, assuming fracture zones of 1.5-m thickness. However, one might expect to find different average values for both the effective porosity and fracture-zone K in this study. The K estimates by Hsieh et al. (1999) were based on a pumping test conducted in a different fracture zone than studied here, and K is expected to vary spatially. Also, this work includes a more detailed description of the K field based on tomographic results.

Parameter Estimation

Calibration of flow and transport models was performed using the UCODE non-linear regression algorithm (Poeter and Hill 1998), which was combined with the finite-element simulation model (Gandhi et al. 2002). The regression procedure iteratively estimates the parameter values that minimize the weighted least-squares error between simulated values and measurements:

$$Z = w_h(s - \hat{s})^2 + w_{\tau^c_{out}}\left(\tau^c_{out} - \hat{\tau}^c_{out}\right)^2 + \sum_{i=1}^{nc} w_c(c_i - \hat{c}_i)^2 \tag{6}$$

where s, $\hat{s}$ are the observed and simulated steady-state drawdown, respectively, at the outlet, $\tau^c_{out}, \hat{\tau}^c_{out}$ are the observed and simulated time of peak concentration, respectively, at the outlet, c_i, $\hat{c}_i$ are the observed and simulated discharge concentrations, respectively, for sample i, w_h, $w_{\tau^c_{out}}$, w_c are the weights on head, peak outlet concentration time, and concentration measurements, respectively, and nc is the number of concentration data used for calibration.

Wagner (1992) demonstrated a procedure to determine weights on different data such that the variance of residuals would be equal for the various types of data. Here, several types of data include only one measurement, precluding variance calculations. Weights were instead selected such that the weighted squared residuals for various data types are, on average, equal (Gailey et al. 1991):

$$w_h\left(h - \hat{h}\right)^2 = w_{\tau^c_{out}}\left(\tau^c_{out} - \hat{\tau}^c_{out}\right)^2 = \frac{1}{nc}\sum_{i=1}^{nc} w_c(c_i - \hat{c}_i)^2 \tag{7}$$

Determination of weights was performed iteratively, by running the calibration, determining new weights such

 DOI 10.1007/s10040-004-0372-y

that [Eq. (7)] is satisfied, and repeating the procedure until convergence.

Evaluation of Alternative Conceptual Models

Interpretation of the difference-attenuation tomograms and measured tracer concentration has led to development of a number of conceptual models for the field data. The purpose of this effort is not to identify a single best-fit model, but rather to identify plausible explanations or rule out unlikely ones. Three conceptual models are considered: (1) homogeneous, (2) heterogeneous, and (3) rate-limited mass transfer (RLMT). A homogeneous model is not expected to match the radar data, but homogeneity is considered to illustrate a possible interpretation of the solute and head data in the absence of geophysical information. The second class of models considers the possibility that channelized transport (Tsang and Tsang 1989) diverts much of the tracer outside the three-well prism, that the anomaly in the FSE2–FSE3 plane represents a slow pathway, and the true concentration peak is not observed in the FSE2–FSE3 tomograms. Heterogeneity in K could thus explain both the apparent discrepancy in peak arrival time and the broadness of the difference-attenuation curves relative to the outlet breakthrough curve. A third candidate explanation for these discrepancies is RLMT. In the presence of RLMT, solute is found in both mobile and immobile domains (e.g., Harvey and Gorelick 1995, 2000). Whereas discharge measurements of concentration preferentially sample from the mobile domain, the radar measurements would be sensitive to salt in either domain, possibly resulting in the observed discrepancy in peak arrival.

The three conceptual models are tested by calibrating each to the available tracer and hydraulic data. Calibration data include (1) tracer concentration at FSE4, (2) the timing of the tracer peak at FSE4, and (3) steady-state hydraulic head at FSE4. After calibration, the simulated breakthrough in the FSE2–FSE3 plane is compared to the difference-attenuation histories of nodes in the plane to check for consistency with the geophysical results.

Direct comparison of estimated difference attenuation and simulated concentration is problematic due to the different spatial and temporal resolution of the two types of information. In transport simulations, the peak arrival time of nodes separated by 0.5 m can vary by more than 10 min, whereas the tomographic results suggest all nodes peak almost simultaneously. The near uniform peak arrival time is a consequence of measurement support volume and tomographic resolution. Small-scale spatial and temporal variability in concentration cannot be captured by the tomography. To compare simulated concentrations with lower-resolution difference-attenuation estimates, an upscaling procedure based on model resolution is presented.

Model resolution is expected to vary spatially in the interwell region due to variable ray density and limited angular coverage (Day-Lewis and Lane 2004). In all rigor, the upscaling procedure should be different for each node. The anomaly in the FSE2–FSE3 plane, however, is confined to a small region, justifying a convenient approximation. The resolution operator for the peak attenuation node is modeled as a weighted average of nodal values in a surrounding space-time neighborhood (8). Based on Fig. 6, nodes within a horizontal distance of 3.5 m and a temporal separation of 20 min are included in the calculation. For the spatial averaging, uniform weights are assumed. The temporal weights were selected based on the resolution of the highest attenuation node relative to the same node in other time steps.

$$\Delta\bar{\alpha}_i^k = \frac{1}{nn}\sum_{l=k-2}^{k+2} w_l \sum_{j=1}^{nn} \Delta\alpha_j^k \tag{8}$$

where $\Delta\bar{\alpha}_i^k$ approximates the difference attenuation estimate at the node i at the k^{th} time, nn is the number of nodes included in the average, w_l are the temporal weights [0.07 0.30 0.40 0.20 0.03], and $\Delta\alpha_j^k$ is the true difference attenuation value at node j at the k^{th} time.

Equation (8) approximates the process whereby tomographic inversion upscales, or smooths, true point values of difference attenuation. Based on this model, an analogous procedure is defined to upscale simulated tracer concentrations for comparison to tomograms:

$$\bar{c}_i^k = \frac{1}{nn}\sum_{l=k-2}^{k+2} w_l \sum_{j=1}^{nn} \Delta c_j^k \tag{9}$$

where $\bar{c}_i^k$ is the upscaled concentration at the node i at the k^{th} time, and c_j^k is the simulated concentration value at node j at the k^{th} time.

Results

The estimates and residuals from the non-linear regression are summarized in Tables 1 and 2, respectively, and the simulated and observed tracer and radar data are shown in Fig. 7. In general, the calibrated models provide

Table 1 Model parameter values. Parameters estimated using non-linear regression are indicated by (*)

Conceptual model/scenario	K_{bv} (m/s)	K_f (m/s)	θ_e	α_L, α_T (m)	K_{high1} (m/s)	K_{high2} (m/s)
1	3.8×10^{-7}	5.5×10^{-7}*	7.4×10^{-4}*	0.029*, 0.0018*	N.A.	N.A.
2/1	3.8×10^{-7}	3.8×10^{-6}*	1.8×10^{-3}*	0.24, 0.08	8.4×10^{-6}*	8.4×10^{-5}*
2/2	1.7×10^{-7}*	6.0×10^{-3}*	5.2×10^{-4}*	0.12, 0.04	N.A.	N.A.
3	3.8×10^{-7}	4.5×10^{-6}	1.4×10^{-3}*	0.06, 0.02	3.2×10^{-4}*	7.9×10^{-5}*

 DOI 10.1007/s10040-004-0372-y

Table 2 Drawdown and concentration residuals from calibrated models

Conceptual model/ scenario	MSE drawdown (m^2)	MSE concentration $(g/L)^2$	MSE peak concentration time $(min)^2$
1	20.0	0.0064	3.4×10^4
2/1	0.46	0.0011	1.8×10^5
2/2	0.0012	0.004	7.3×10^4
3	2.13	0.0016	1.4×10^5

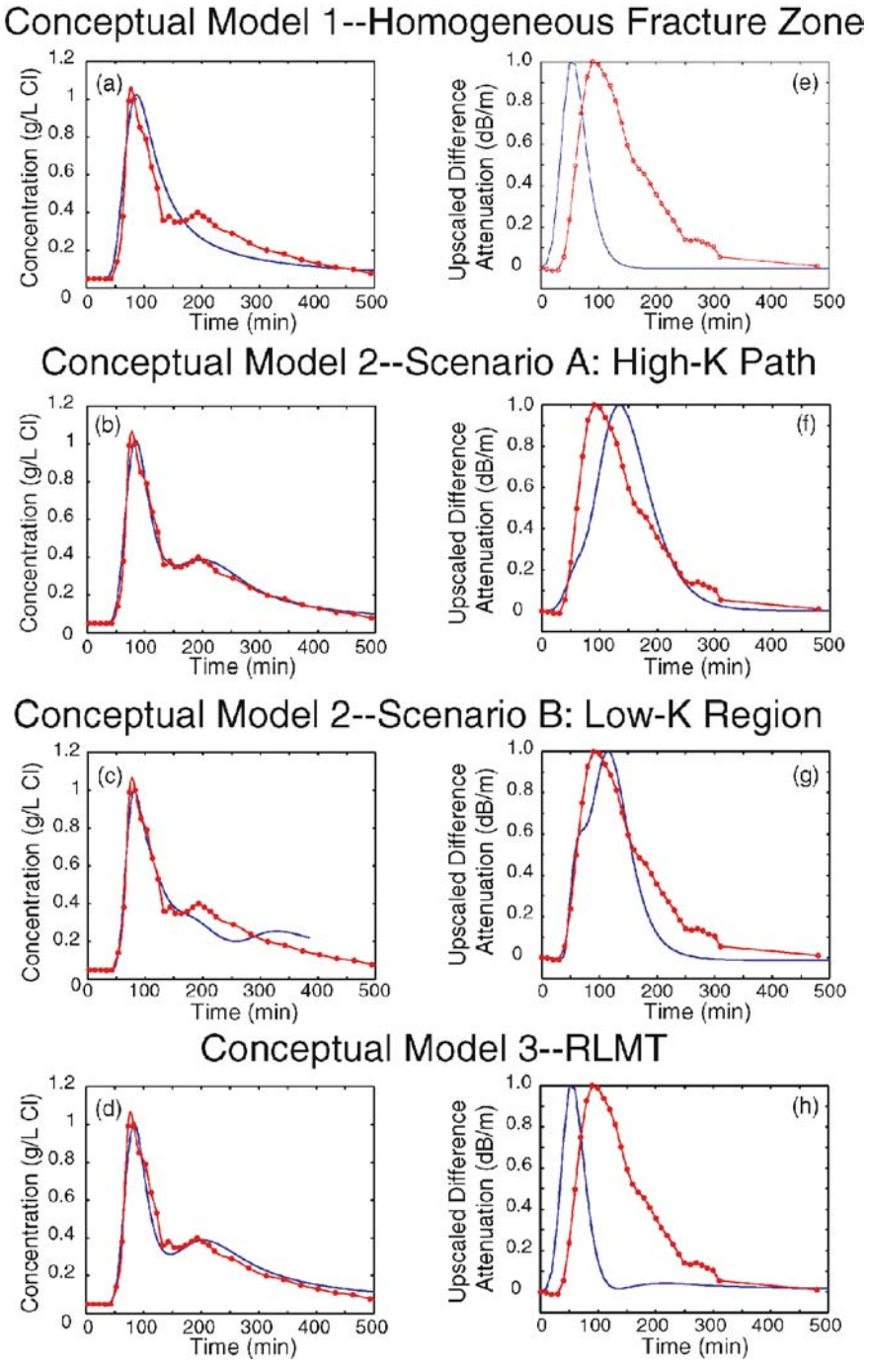

Fig. 7. a–d Simulated (*blue*) and observed (*red*) outlet concentration histories for calibrated conceptual models. **e–h** Normalized, simulated upscaled concentration (*blue*) and observed difference-attenuation (*red*) for calibrated conceptual models

DOI 10.1007/s10040-004-0372-y

reasonable reproductions of the tracer data. Given the simplifications and approximations involved in the upscaling procedure [Eq. (9)], it is unreasonable to expect the upscaled concentration history to match the observed radar difference-attenuation curve exactly; however, several models successfully explain the apparent discrepancy in the timing of peak difference attenuation.

Conceptual Model 1: Homogeneous K-field

Although extreme heterogeneity is expected in fractured rock, in the absence of geophysical data one might assume the fracture zone to be a homogeneous high-*K* layer. This would constitute a reasonable and parsimonious interpretation of the available hydraulic and tracer data. Estimated parameters include (1) effective porosity, (2) the homogeneous *K* of the fracture zone, (3) longitudinal dispersivity, and (4) transverse dispersivity.

Calibration of the homogeneous fracture-zone model results in a poor match to the observed discharge concentration (Fig. 7a). Specifically, the observed secondary peak is not present in the simulated concentration history, and the magnitude and timing of the first peak are not matched. Furthermore, the simulated peak difference attenuation occurs too early (Fig. 7e). The non-linear regression yields estimates for the vertical *K* of the bedrock, the isotropic *K* of the fracture zone, and the longitudinal and transverse dispersivities, which are reported in Table 1; residuals are listed in Table 2. This scenario represents a benchmark against which to measure the value of incorporating geophysical information. Without knowledge of the course or timing of tracer migration, the homogeneous case would be the simplest working hypothesis.

Conceptual Model 2: Heterogeneity in K

Heterogeneity in *K* is an obvious explanation for the apparent discrepancy between radar and tracer data. Two scenarios are considered, each representing spatial variations in *K* that could divert tracer mass outside the tomographic image planes. This hypothesis is consistent with the location of the difference-attenuation anomaly in the FSE2–FSE3 plane. Solute traveling along an unseen fast path could arrive at the outlet ahead of the solute detected in the FSE2–FSE3 plane, thus explaining the discrepancy in the timing of the difference attenuation and concentration peaks. Moreover, the observed difference-attenuation anomaly, corresponding to a slower flow path, could exhibit a broader peak than the first peak at the outlet. Under this hypothesis, the tracer observed in the FSE2–FSE3 plane would contribute to the second peak at the outlet.

Severe heterogeneity and preferential flow are expected in fractured rock. Transport along preferential pathways may result from fracture channels, elongate regions of enhanced fracture aperture that occur at fracture intersections or as a consequence of shearing (National Research Council 1996, pp. 273–274). Even in the absence of such features, channelized transport can occur in variable-aperture fractures due to the non-uniform velocity field (Tsang and Tsang 1989). Although the fracture zone studied can be treated as homogeneous with regard to hydraulic data (Day-Lewis et al. 2000), solute-transport data are more sensitive to the effects of heterogeneity.

Two heterogeneous fracture-zone *K*-fields are considered: (1) a high-*K* pathway just outside the FSE2–FSE3 plane (Fig. 8a), and (2) a low-*K* zone that diverts tracer outside the FSE2–FSE3 plane (Fig. 8b). The high-*K* feature in (1) represents a fracture channel, whereas the low-K feature in (2) represents a local decrease in permeability — in effect a plug in the fracture zone. The two *K*-field zonations are qualitatively consistent with the spatial location of the geophysical anomaly. Consistency with the timing of peak attenuation is evaluated based on upscaled simulated concentrations from the calibrated model.

Heterogeneity scenario A: high-K path outside the FSE2–FSE3 plane

Under this hypothesis, a high permeability pathway is embedded within the fracture zone identified by Hsieh and Shapiro (1996; Fig. 8a). Tracer, unseen by the geophysics, contributes to the first concentration peak at FSE4. Tracer that migrates through the transition zone, shown in yellow in Fig. 8a, corresponds to the attenuation peak in the FSE2–FSE3 plane and results in the secondary peak in discharge concentration. The zone of intermediate *K* proved useful for diverting tracer away from the middle of the FSE2–FSE3 plane for consistency with the radar information. Without the transition zone, much of the tracer mass traveled directly between the injection and extraction wells along slow paths through the middle of the FSE1–FSE4 region. Due to the nature of the doublet tracer test, large contrasts in *K* are necessary to divert tracer away from the middle of the FSE2–FSE3 plane.

The estimated parameters for this scenario include (1) effective porosity, (2) the *K* of the fracture zone, (3) the *K* of the transition zone, and (4) the *K* of the high-*K* path. Resulting parameter estimates and residuals are reported in Tables 1 and 2, respectively. The simulated discharge concentration is shown in Fig. 7b. For this scenario, the estimate of effective porosity is substantially higher than for the homogeneous case. This is a consequence of representing more heterogeneity than was considered for the homogeneous model. Previously a lower effective porosity was necessary to move the tracer quickly to the outlet. The presence of the high-*K* zone has a similar result.

The match to the outlet tracer concentration history for this scenario (Fig. 7b) is superior to the match from scenario 1 (Fig. 7a). In particular, the secondary peak and tail are better reproduced, and the timing of peak concentration in the FSE2–FSE3 plane is more consistent with the radar data (Fig. 7f). As observed in the field data, the peak concentration at the outlet occurs earlier than the peak upscaled concentration in the image plane.

 DOI 10.1007/s10040-004-0372-y

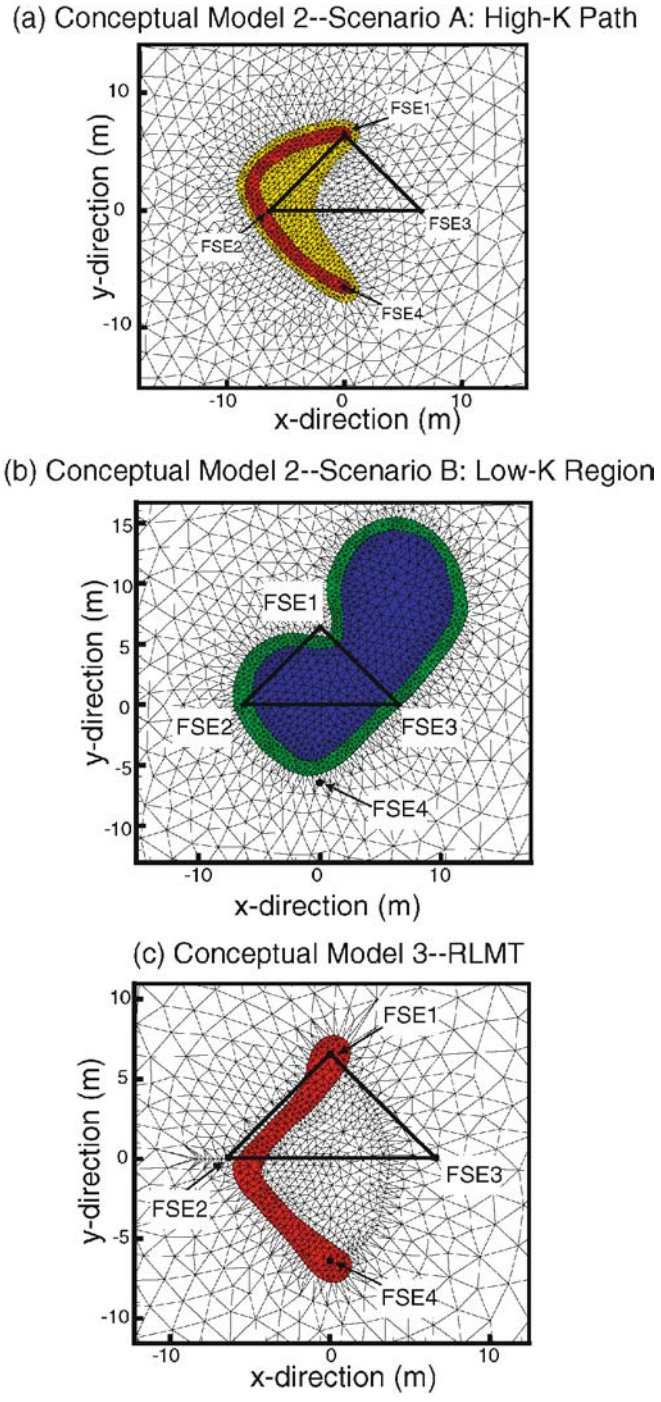

Fig. 8 Configuration of the high-*K* pathway (*red*) in **a** conceptual model 2: scenario A, **b** conceptual model 2: scenario B, and **c** conceptual model 3. The tomographic image planes are shown as *black lines* between well pairs. *Blue* indicates low *K*, *green and yellow* intermediate *K*, and *red* high *K*

Heterogeneity scenario B: low-K region

In this scenario, tracer is diverted toward FSE2 due to the presence of a low-*K* region in between the wells (Fig. 8b). The *K* of this region is set equal to that of the surrounding low-*K* bedrock, thus the region is a plug in the fracture zone, corresponding to a region of unconnected, closed, or otherwise impermeable fractures. To avoid numerical oscillations, the model includes a boundary region of intermediate *K* around the low-*K* region, shown in green in Fig. 8b. This region has a *K* set equal to one order of magnitude less than the value for the fracture zone. Estimated parameters are (1) effective porosity, (2) the vertical *K* of the bedrock, and (3) the *K* of the fracture zone. The parameter estimates and residuals are reported in Tables 1 and 2, respectively. The match to the discharge concentration is shown in Fig. 7c. The match to the outlet data is not as good as for the high-K path scenario. The secondary peak and tailing behavior are not accurately reproduced; however, simulated concentration breakthrough in the FSE2–FSE3 plane suggests that the presence of a low-*K* feature in the interwell domain might also explain the timing of the radar peak (Fig. 7g).

Conceptual Model 3: Rate-Limited Mass Transfer

In fractured rock, first-order RLMT can be used to represent mass transfer between water in open fractures and stagnant water in dead-end fractures or in the rock matrix. These mechanisms are thought to be responsible for fat tails observed in tracer tests at fractured-rock sites, although Becker and Shapiro (2000) showed evidence that slow advection and not diffusive mass transfer is responsible for tailing behavior at the Mirror Lake Site.

Under first-order RLMT (Harvey and Gorelick 1995, 2000), solute mass diffuses between mobile and immobile domains according to first-order kinetics [Eq. (5a)]. Direct concentration measurements preferentially sample from the mobile domain, whereas radar attenuation would be sensitive to salt in either domain. Thus, the shape of the difference-attenuation breakthrough curve may differ from that of the sampled tracer breakthrough curve in timing and shape. First-order RLMT might also explain the double peak. Several researchers have shown that, under first-order RLMT, a double peak can develop even in the absence of heterogeneity (Bellin et al. 1991; Harvey and Gorelick 1995). For comparison to difference attenuation, the appropriate quantity is the sum of mobile and immobile concentrations, each weighted by its respective fraction of total porosity:

$$C_T = \frac{\theta_m C_m + \theta_{im} C_{im}}{\theta_m + \theta_{im}} \tag{10}$$

A single-path model consistent with the location of the radar anomaly in the FSE2–FSE3 plane is considered (Fig. 8c). Under advective-dispersive transport, this model could not produce results consistent with the late timing of radar breakthrough in the FSE2–FSE3 plane. With RLMT, however, it is possible for the peak of C_T to occur later than the peak of C_m. In this scenario, estimated parameters include (1) the immobile-domain porosity, (2) mass-transfer rate coefficient, (3) the *K* of the pathway, (4) the *K* of the fracture zone, and (5) the vertical *K* of the low-*K* bedrock. The immobile porosity was estimated to be $5.7\text{x}10^{-4}$, and the rate coefficient 0.13 s^{-1}; other parameter estimates are reported in Table 1. The resulting

 DOI 10.1007/s10040-004-0372-y

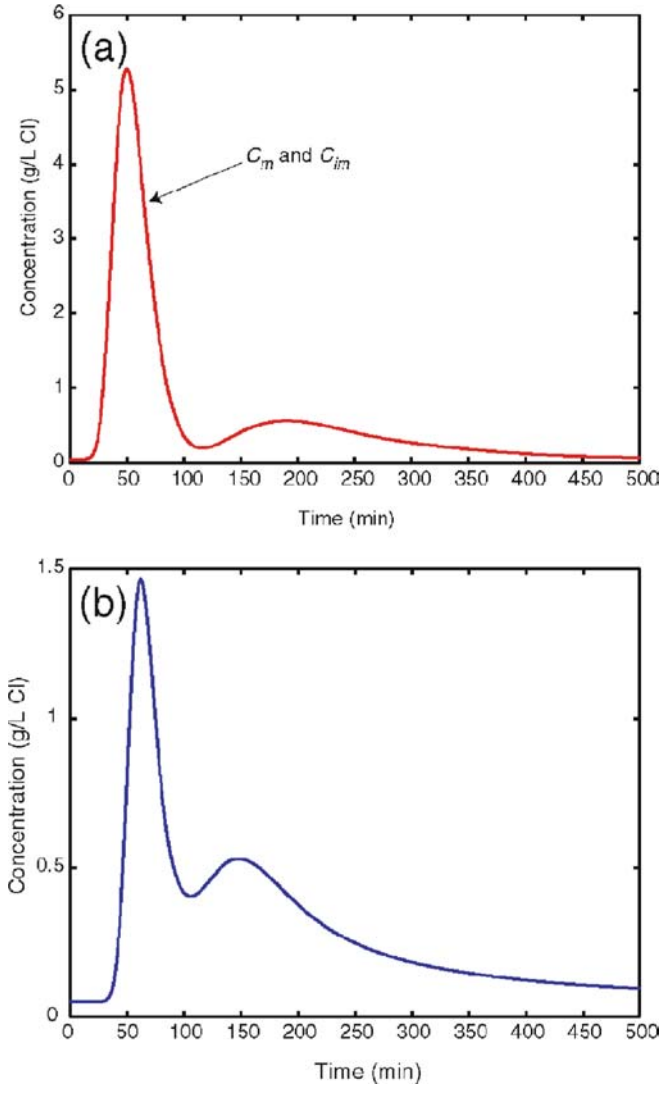

Fig. 9. a Simulated mobile and immobile concentration histories for the RLMT one-path model in the FSE2–FSE3 plane at x=–5 m. The two concentrations are in near equilibrium. **b** Simulated outlet concentration without RLMT

match to the solute data is qualitatively good (Fig. 7d), but the match to radar information is not (Fig. 7h). The mobile, immobile and total concentrations at locations in the FSE2–FSE3 plane are nearly identical (Fig. 9a), and there is virtually no time lag between the peak of C_m and C_T. Thus, the non-linear regression converged to RLMT parameters such that mobile and immobile concentrations are in near equilibrium.

It is interesting to note that the second peak and tail in the outlet concentration history for this scenario results not from RLMT, but from K heterogeneity. Given the calibrated parameter estimates for K and θ_m, advective-dispersive transport is simulated without RLMT for the one-path model, obtaining the outlet concentration shown in Fig. 9b. The second peak derives from tracer that travels by slow advection a short distance through the lower-K fracture zone before entering the high-K pathway. RLMT serves mainly to retard and decrease the mobile concentration. Apparently, the degree of heterogeneity included in the model is sufficient to reproduce much of the breakthrough curve without RLMT, and inclusion of more heterogeneity would "fatten" the tail further.

Discussion and Conclusions

An integrated interpretation of difference-attenuation radar, tracer, and hydraulic data was demonstrated for field data from a fractured-rock site. A suite of numerical models was constructed based on the geophysical data and calibrated using non-linear regression to head, concentration, and tracer peak travel time. Several hydraulic conductivity zonations were identified that could explain, qualitatively, the observed radar and hydrologic data. The seeming discrepancy between the timing of the difference-attenuation peak and tracer concentration measured at the outlet can be explained by simple zonal K heterogeneity. The observed solute concentration history, including a double peak, was reproduced without invoking rate-limited mass transfer. Modeling results indicate that channelized transport within a high-K fracture zone likely transmits tracer outside the tomographic image planes.

Although the K-fields identified by the non-linear regression are non-unique, and other models could match the data equally well, this work demonstrates the value of combining geophysical monitoring and conventional hydrologic characterization. In the absence of geophysical information, a homogeneous model might serve to explain much of the solute and hydraulic data. The incorporation of time-lapse radar data greatly facilitated the interpretation of traditional hydrologic measurements by constraining the number of plausible hypotheses. A broader range of plausible K-fields could be explored using stochastic inversion (Wagner and Gorelick 1989; Harvey and Gorelick 1995; Kitanidis 1995; Rama Rao et al. 1995; Wen et al. 1996); however, this would be far more computationally intensive, and is outside the scope of the present study.

The principal contributions of this work were (1) a demonstration of combining time-lapse geophysical data and conventional hydrologic characterization and model calibration, (2) development and application of an upscaling procedure to facilitate comparison of simulated or measured concentrations with lower resolution tomographic estimates, and (3) site-specific insights into heterogeneity of hydraulic conductivity and possible solute channeling in fractured rock. The use of difference-attenuation radar tomograms as surrogate concentration data holds great promise for facilitating the construction and calibration of flow and transport models; however, upscaling procedures may be required to relate tomograms to solute concentration. Depending on the radar wavelength, data error, and transmitter-receiver geometry, inverted difference-attenuation values will represent local averages, whereas simulated (or measured) con-

 DOI 10.1007/s10040-004-0372-y

centrations approximate point values. Further work is necessary to fully couple a forward model for radar tomography with inverse models for flow and transport, based on (1) an effective-medium model to relate attenuation changes to changes in concentration, and (2) the resolution matrix for the tomographic inversion.

Acknowledgments This material is based upon work supported by the National Science Foundation under Grant Nos. EAR-0124262 and EAR-9705812. Any opinions, findings, and conclusions or recommendations expressed in this material are those of the author(s) and do not necessarily reflect the views of the National Science Foundation. Additional support was provided by the US Geological Survey Toxic Substances Hydrology Program and the US Environmental Protection Agency through EPA STAR Fellowship U-915155-01-0.

References

Archie GE (1942) The electrical resistivity log as an aid in determining some reservoir characteristics. Trans Am Inst Mineral Metall Petrol Eng 146:54–62

Becker MW, Shapiro AM (2000) Tracer transport in fractured crystalline rock: evidence of non-diffusive breakthrough tailing. Water Resour Res 36:1677–1886

Becker MW, Shapiro AM (2003) Interpreting tracer breakthrough tailing from different forced-gradient tracer experiment configurations in fractured bedrock. Water Resour Res 39:1024, Doi:10.1029/2001WR001190

Bellin A, Valocchi A, Rinaldo A (1991) Double peak formation in reactive solute transport in one-dimensional heterogeneous porous columns. Quaderni del dipartimento IDR, Dipartimento di Ingegrneria Civile ed Ambientale, Universita degli Studi di Trento

Binley A, Henry-Poulter S, Shaw B (1996) Examination of solute transport in an undisturbed soil column using electrical resistance tomography. Water Resour Res 32:763–769

Binley A, Winship P, Middleton R, Pokar M, West J (2001) High resolution characterization of vadose zone dynamics using cross-borehole radar. Water Resour Res 37:2639–2652

Day-Lewis FD, Lane JW Jr (2004) Assessing the resolution-dependent utility of tomograms for geostatistics. Geophys Res Lett 31:L07503, Doi: 10.1029/2004GL019617

Day-Lewis FD, Hsieh PA, Gorelick SM (2000) Identifying fracture-zone geometry using simulated annealing and hydraulic-connection data. Water Resour Res 36:1701–1721

Day-Lewis FD, Harris JM, Gorelick SM (2002) Time-lapse inversion of crosswell radar data. Geophysics 67:1740–1752

Day-Lewis FD, Lane JW Jr, Harris JM, Gorelick SM (2003) Time-lapse imaging of saline-tracer transport in fractured rock using difference-attenuation radar tomography. Water Resour Res 39:1290 Doi: 10.1029/2002WR001722

Dines KA, Lytle RJ (1979) Computerized geophysical tomography. Proc. Inst Electrical Electronics Eng 67:1065–1073

Ellefsen KJ, Hsieh PA, Shapiro AM (2002) Crosswell seismic investigation of hydraulically conductive, fractured bedrock near Mirror Lake, New Hampshire. J Appl Geophys 50:299–317

Gailey RM, Gorelick SM, Crowe AS (1991) Coupled process parameter estimation and prediction uncertainty using hydraulic head and concentration data. Advance Water Resour 14:301–314

Gandhi RK, Hopkins GD, Goltz MN, Gorelick SM, McCarty PL (2002) Fullscale demonstration of in-situ cometabolic biodegradation of trichloroethylene in groundwater, 1: dynamics of a recirculating well system. Water Resour Res 38:9-1–9-6

Harvey CF, Gorelick SM (1995) Temporal moment-generating equations: modeling transport and mass transfer in heterogeneous aquifers. Water Resour Res 31:1895–1911

Harvey CF, Gorelick SM (2000) Rate-limited mass transfer or macrodispersion; which dominates plume evolution at the macrodispersion experiment (MADE) site? Water Resour Res 36:637–650

Hsieh PA, Shapiro AM (1996) Hydraulic characteristics of fractured bedrock underlying the FSE well field at the Mirror Lake Site, Grafton County, New Hampshire. In: Morganwalp DW, Aronson DA (eds) US Geological Survey Toxic Substances Hydrology Program: Proceedings of the technical meeting, Colorado Springs, Colorado, 20–24 September 1993. US Geol Surv Water-Resour Invest Rept 94-4015, vol 1:127–130

Hsieh PA, Shapiro AM, Tiedeman CR (1999) Computer simulation of fluid flow in fractured rocks at the Mirror Lake FSE well field. In: Morganwalp DW, Buxton HT (eds) US Geological Survey Toxic Substances Hydrology Program: Proceedings of the Technical Meeting, Charleston, South Carolina, 8–12 March 1999, Subsurface Contamination from Point Sources. US Geol Surv Water-Resour Invest Rept 99-4018C, pp 777–781

Hubbard S, Chen J, Peterson J, Majer E, Williams K, Swift D, Mailliox B, Rubin Y (2001) Hydrogeological characterization of the DOE bacterial transport site in Oyster Virginia using geophysical data. Water Resour Res 37:2431–2456

Kitanidis PK (1995) Quasi-linear geostatistical theory for inversing. Water Resour Res 31:2411–2419

Lane JW Jr, Haeni FP, Day-Lewis FD (1998) Use of time-lapse attenuation-difference radar tomography methods to monitor saline tracer transport in fractured crystalline bedrock, In: Seventh International Conference on Ground Penetrating Radar, Lawrence, KS, 27–30 May, pp 533–538

Lane JW Jr, Day-Lewis FD, Harris JM, Haeni FP, Gorelick SM (2000) Attenuation-difference radar tomography: results of a multiple-plane experiment at the US Geological Survey fractured rock research site, Mirror Lake, New Hampshire. In: Noon DA, Stickely GF, Longstaff D (eds) Eighth International Conference on Ground Penetrating Radar, SPIE vol 4084

Menke W (1989) Geophysical data analysis: discrete inverse theory, revised edn. Academic Press, San Diego

National Research Council (1996) Rock fractures and fluid flow. Natl Acad Press, Washington, DC

Nolet G (1987) Seismic tomography. D. Reidel Publishing, Dordrecht

Olsson O, Anderson P, Gustafsson E (1991) Site characterization and validation: -monitoring of saline tracer transport by borehole radar measurements, final report, Stripa project TR91-18, Swedish Nuclear Fuel and Waste Management Co., Stockholm

Olsson O, Falk L, Forslund O, Lundmark L, Sandberg E (1992) Borehole radar applied to the characterization of hydraulically conductive fracture zones in crystalline rock. Geophys Prospect 40:109–142

Poeter EP, Hill MC (1998) Documentation of UCODE, a computer code for universal inverse modeling. US Geol Surv Water-Resour Invest Rept 98-4080

Rama Rao BS, LaVenue AM, de Marsily G, Marietta MG (1995) Pilot point methodology for automated calibration of an ensemble of conditionally simulated transmissivity fields. Water Resour Res 31:475–493

Schuster GT (1996) Resolution limits for crosswell migration and traveltime tomography. Geophys J Int 127:427–440

Shapiro A (1996) Estimation of effective porosity in fractured crystalline rock by controlled tracer tests. Joint US geological survey. US Nuclear Regulatory Commission Workshop on Research Related to Low-level Radioactive Waste Disposal, pp 185–190

Shapiro A (2001) Effective matrix diffusion in kilometer-scale transport in fractured crystalline rock. Water Resour Res 37:507–522

Slater L, Binley AM, Daily W, Johnson R (2000) Cross-hole electrical imaging of a controlled saline tracer injection. J Appl Geophys 44:85–102

Tiedeman CR, Hsieh PA (2001) Assessing an open-well aquifer test in fractured crystalline rock. Ground Water 39:68–78

Tiedeman CR, Goode DJ, Hsieh PA (1998) Characterizing a ground water basin in a New England mountain and valley terrain. Ground Water 36:611–620

Tsang YW, Tsang CF (1989) Flow channeling in a single fracture as a two-dimensional strongly heterogeneous permeable medium. Water Resour Res 25:2076–2080

Vasco DW, Datta-Gupta A, Long JCS (1997) Resolution and uncertainty in hydrologic characterization. Water Resour Res 33:379–397

Wagner BJ (1992) Simultaneous parameter estimation and contaminant source characterization for coupled groundwater flow and contaminant transport modelling, J Hydrol 35:275–303

Wagner BJ, Gorelick SM (1989) Reliable aquifer remediation in the presence of spatially-variable hydraulic conductivity: from data to design. Water Resour Res 25:2211–2225

Wen Xian-Huan, Gomez-Hernandez J, Capilla JE, Sahuquillo A (1996) Significance of conditioning to piezometric head data for predictions of mass transport in groundwater modeling. Math Geol 28:951–968

 DOI 10.1007/s10040-004-0372-y